ACS APPLIED POLYMER MATERIALS

pubs.acs.org/acsapm

Article

Ensemble-Dependent Diffusivity Selectivity in Amorphous Polyethylene: A Statistically Validated Molecular Dynamics Study of H_2/CH_4 Transport

Daniel Delgado-Uriarte* and Alejandro Lopez*

Cite This: *ACS Appl. Polym. Mater.* 2026, 8, 8017−8031

Read Online

ACCESS | Metrics & More | Article Recommendations | Supporting Information

ABSTRACT: The integration of hydrogen into natural gas networks (H_2NG) demands a rigorous understanding of relative gas transport properties in polymeric infrastructure to mitigate risks such as leakage and Rapid Gas Decompression (RGD). Polyethylene (PE) is a critical material for this transition due to its resistance to hydrogen embrittlement, yet its susceptibility to gas permeation remains a safety concern. In this work, we present a fully open-source, statistically validated Molecular Dynamics (MD) framework to quantify the *diffusive* transport of H_2 and CH_4 in amorphous polyethylene. Using the TraPPE-UA force field and a multistage high-pressure annealing protocol, we generated dense, well-equilibrated matrices (pure-polymer reference ρ_{pure} = 0.814 ± 0.001 g cm^{-3} and mix systems at $\rho_{Mix,NPT}$ = 0.803 ± 0.001 and $\rho_{Mix,NVT}$ = 0.819 ± 0.003 g cm^{-3}) and characterized them using radial distribution functions, the full pore size distribution, and the standard porous-materials descriptors LCD (Largest Cavity Diameter) and PLD (Pore Limiting Diameter). Diffusion coefficients of H_2 and CH_4 were extracted from 48 independent production simulations (3 seeds × 2 systems × 2 ensembles × 4 temperatures) over the range 298−373 K under both isobaric (NPT, P = 1 atm) and isochoric (NVT) ensembles. Our central finding is an *ensemble-dependent diffusivity-selectivity trade-off*: thermal expansion in NPT conditions opens the free-volume network and reduces the H_2/CH_4 *diffusivity* selectivity α_D from ∼4.8 at 298 K to ∼1.9 at 373 K, whereas volumetric confinement (NVT) suppresses the free-volume dilation and yields a far more gradual decrease ($\alpha_D \approx 4.6 \rightarrow 2.5$). When the eight $D(T)$ data points for each gas are pooled into a Cohen−Turnbull plot of ln D versus $1/FV_0$ (matrix void fraction), the NPT and NVT data collapse onto a single master line per gas with slopes whose ratio matches the squared kinetic-diameter ratio $(\sigma_{CH_4}/\sigma_{H_2})^2 \approx 1.73$. This collapse provides direct quantitative evidence that the apparent ensemble dependence of selectivity is governed by free-volume modulation alone and that the activation parameter γv^* scales with the cross-sectional area of the penetrant. Trajectory analysis further confirms an activated-hopping mechanism for H_2 with a broad displacement distribution, while CH_4 dynamics are dominated by cage rattling. We explicitly distinguish the diffusivity selectivity α_D reported here from the experimental permeability selectivity $\alpha_P = \alpha_D \times \alpha_S$, noting that for H_2/CH_4 in PE the solubility selectivity $\alpha_S < 1$ and therefore $\alpha_P < \alpha_D$. The combination of statistically validated diffusivities, density-resolved free-volume metrics, and the Cohen−Turnbull master curve provides a transferable framework for assessing how thermomechanical boundary conditions modulate the kinetic sieving behavior of polymer infrastructure exposed to hydrogen−methane mixtures.

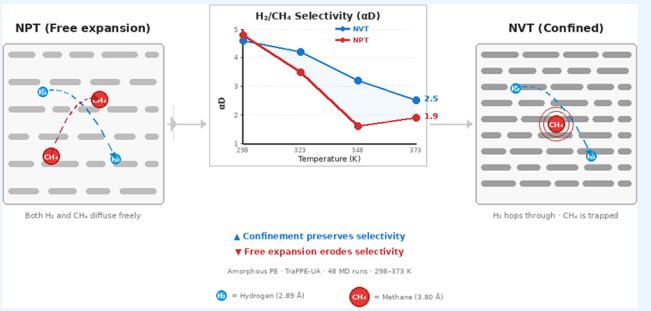

KEYWORDS: *molecular dynamics, polyethylene, hydrogen transport, diffusivity selectivity, free volume, TraPPE-UA*

1. INTRODUCTION

The global transition toward a decarbonized energy economy has positioned hydrogen as a key energy carrier. To accelerate its deployment, the strategy of blending hydrogen into existing natural gas grids (H_2NG) is being widely adopted as a transitional solution to reduce carbon intensity without requiring immediate, complete infrastructure replacement.[1−5] However, the compatibility of legacy infrastructure with hydrogen-rich mixtures presents significant material challenges. While metallic pipelines are susceptible to hydrogen embrittlement,[6,7] Polyethylene (PE) pipelines-which constitute the backbone of low-pressure gas distribution networks-offer superior chemical resistance and lower installation costs.[8] Nevertheless, PE components are particularly susceptible to gas permeation compared to metallic counterparts.[9,10]

Received: January 22, 2026
Revised: April 15, 2026
Accepted: May 6, 2026
Published: May 30, 2026

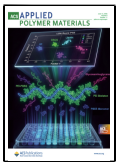

Recent studies highlight specific safety risks associated with H_2NG transport in polymers. The permeability coefficient ($P = S \times D$) of hydrogen in PE is significantly higher than that of methane, a phenomenon attributed primarily to the much higher diffusivity of H_2 due to its smaller kinetic diameter.[11] This preferential permeation raises concerns regarding leakage, energy loss, and the potential for localized accumulation of flammable mixtures.[12,13] Furthermore, the interaction of high-pressure hydrogen with the polymer matrix can compromise structural integrity. A critical safety concern is the phenomenon of Rapid Gas Decompression (RGD), commonly referred to as "blistering".[9,14] This failure mechanism manifests when polymeric materials, saturated with high-pressure gas, undergo sudden depressurization. Due to the solubility of gases in the amorphous regions, the dissolved gas expands violently within the polymer's free volume voids before it can diffuse out, leading to irreversible mechanical damage.

Understanding the diffusive mobility of dissolved gases is, therefore, essential not only for leakage estimation but also for defining safe decompression protocols. The transport of light gases in rubbery and glassy polymers is generally described by the solution-diffusion mechanism.[9,15] In this framework, permeability (P) is defined as the product of solubility (S) and diffusivity (D):

$$P = S \times D \tag{1}$$

While macroscopic experiments provide bulk permeability data, they often lack the microscopic resolution required to understand the relative transport properties of different gas species within the polymer matrix. Molecular Dynamics (MD) simulations have emerged as a powerful tool to resolve diffusion mechanisms at the atomistic scale.[16−19]

However, a survey of the recent literature reveals two recurring methodological limitations that compromise the reliability of many computational studies. First, the generation of amorphous polymer structures often suffers from insufficient equilibration. Standard protocols may leave excess free volume or residual chain ordering, leading to artificially inflated diffusion coefficients that do not correspond to realistic, well-annealed materials.[20] Second, statistical sampling is frequently inadequate. In dense polymers above T_g, gas transport is dominated by rare "activated hopping" events rather than continuous liquid-like diffusion, a process intrinsically linked to the redistribution of free volume elements.[21,22] Capturing these rare events requires long simulation time scales and rigorous uncertainty quantification, which are often absent in single-trajectory studies.

Moreover, most computational studies focus exclusively on relaxed bulk systems under constant pressure (NPT). This neglects the effects of mechanical confinement that may arise in various practical scenarios-for example, from crystalline lamellae constraining the amorphous phase in semicrystalline PE, from rigid housings in compressed joints, or from reinforcing fillers. A volumetrically constrained polymer can be thermodynamically approximated by the canonical (NVT) ensemble. The impact of this confinement on H_2/CH_4 diffusivity selectivity has not been systematically quantified.[23]

In this work, we address these gaps by developing a rigorous, fully open-source Molecular Dynamics framework to quantify diffusion coefficients and diffusivity selectivity in dense amorphous polyethylene. We implement a multistage high-pressure annealing protocol to ensure structural convergence and use the TraPPE-UA force field[24] to accurately describe polymer-gas interactions. By performing a systematic comparison of 48 independent simulations of H_2/CH_4 mixtures, we quantify the interplay between thermal expansion (NPT) and volumetric confinement (NVT), revealing an ensemble-dependent diffusivity selectivity trade-off with implications for understanding gas transport in polymer infrastructure.

The scope of this study focuses on the diffusive component of transport (D) in the amorphous phase of PE, with the following considerations regarding real-world applications:

1 **Amorphous Phase Transport:** Since crystalline lamellae in polyethylene are essentially impermeable to light gases,[11] permeation through semicrystalline PE is governed by the transport properties of the amorphous regions, modulated by a geometric tortuosity factor typically described by Maxwell or Nielsen models.[25] By isolating a dense, equilibrated amorphous domain, we characterize the intrinsic diffusive mobility relevant to the conductive phase of HDPE/LDPE.
2 **Ensemble-Dependent Boundary Conditions:** The NPT and NVT ensembles represent two limiting thermomechanical boundary conditions. NPT corresponds to unconstrained expansion, as in a free polymer liner. NVT represents perfect volumetric confinement, which may arise from crystalline constraints in semicrystalline PE, rigid housings in compressed joints, or reinforcing fillers. Our comparative analysis quantifies how these boundary conditions affect H_2/CH_4 diffusivity selectivity.

2. MATERIALS AND METHODS

2.1. Molecular Dynamics Protocol

All simulations were performed using the LAMMPS software package.[26] The equations of motion were integrated using the standard velocity-Verlet algorithm, a robust approach widely validated for polymer transport studies.[12,17,27] A time step of $\Delta t = 1$ fs was selected to ensure energy conservation for the fast degrees of freedom associated with hydrogen molecules, consistent with previous diffusion benchmarks.[16,28]

Nonbonded interactions were truncated at a cutoff distance of 10.0 Å, with standard analytic tail corrections applied to energy and pressure terms to account for the homogeneity of the bulk matrix.[29] Neighbor lists were updated every 10 steps using a binning algorithm with a skin distance of 2.0 Å.[27]

Temperature and pressure were controlled using deterministic extended-system formalisms. For constant temperature simulations (both NVT and NPT ensembles), the Nosé-Hoover thermostat was employed.[30,31] For constant pressure simulations (NPT), the isotropic Parrinello−Rahman barostat was utilized.[32] Damping parameters were set to 100 and 1000 fs, respectively. These coupling constants correspond to the standard recommendations of 100 and 1000 integration time steps for the LAMMPS software,[26] selected to ensure stable thermodynamic sampling without interfering with the natural vibrational frequencies of the polymer chains.

2.2. Force Field Definition

The polyethylene (PE) matrix and penetrant gases were modeled using the Transferable Potentials for Phase Equilibria—United Atom (TraPPE-UA) force field.[24] This force field was originally parametrized to reproduce the critical temperatures and saturated liquid densities of *n*-alkanes, and has been shown to effectively describe the structural properties of amorphous polymers in transport studies.[18]

In this formalism, CH_x groups are treated as single interaction centers (pseudoatoms), a coarse-graining approach that reduces the computational cost by an order of magnitude compared to all-atom models while retaining thermodynamic accuracy.[24] Methane (CH_4) was modeled using this same united-atom representation, consistent with the polymer backbone formalism.[18,24]

https://doi.org/10.1021/acsapm.6c00287
ACS Appl. Polym. Mater. 2026, 8, 8017−8031

Nonbonded interactions were described by the pairwise-additive Lennard-Jones 12−6 potential:

$$U_{LJ}(r_{ij}) = 4\varepsilon_{ij}\left[\left(\frac{\sigma_{ij}}{r_{ij}}\right)^{12} - \left(\frac{\sigma_{ij}}{r_{ij}}\right)^{6}\right] \quad (2)$$

The Lennard-Jones parameters (ε_{ii} and σ_{ii}) for the polymer units and methane were taken directly from the TraPPE parameter set.[24] Hydrogen (H_2) was modeled as a rigid diatomic molecule, with center-of-mass parameters adapted to reproduce transport properties in hydrocarbons.[18] Cross-interactions between different species (e.g., polymer gas) were computed using standard Lorentz−Berthelot mixing rules.[27,33]

Intramolecular interactions included harmonic bond stretching and angle bending. For polyethylene, dihedral rotation was governed by the OPLS (Optimized Potentials for Liquid Simulations) united-atom torsional potential adopted by TraPPE.[24,34] This potential is essential to strictly enforce the conformational statistics of the backbone (such as trans/gauche ratios), which dictate the chain flexibility and free volume distribution. A complete summary of all simulation parameters and algorithms is provided in Table 1.

Table 1. Summary of Simulation Parameters and Algorithms[a]

Parameter/Method	Value/Setting	Justification/Reference
Software	LAMMPS (Stable release)	Plimpton[26]
Force Field (Polymer/Gas)	TraPPE-UA	Martin & Siepmann[24]
Integration Algorithm	Velocity-Verlet	Standard symplectic integrator[35]
Time Step (Δt)	1 fs	Conservation of energy for H-bonds[28]
Cutoff Radius (r_c)	10.0 Å	TraPPE standard recommendation[24]
Long-range Corrections	Analytic Tail Corrections	Homogeneity assumption for bulk fluids
Thermostat	Nosé−Hoover	Canonical sampling[30]
Thermostat Damping	100 fs (100Δt)	LAMMPS standard recommendation[26]
Barostat	Parrinello-Rahman	Isobaric sampling[32]
Barostat Damping	1000 fs (1000Δt)	LAMMPS standard recommendation[26]
Nonbonded Neighbor List	Binning (r_c + 2.0 Å)	Computational efficiency

[a]References indicate the source of the parameter value or the standard recommendation for the chosen method.

2.3. System Generation and High-Pressure Equilibration

A critical challenge in simulating amorphous polymers is generating a realistic structure with the correct density and chain packing. Insufficient equilibration often leads to "microvoids" that artificially inflate diffusion coefficients.[36,37] To address this, we implemented a multistage protocol inspired by the high-pressure annealing techniques described by Zheng et al.:[12]

1 **Initial Generation:** A low-density system containing 50 linear chains of 100 carbon backbone atoms each (C_{100}, corresponding to $M_w \approx 1400$ g/mol) was generated using a self-avoiding random walk (SARW) algorithm to prevent initial overlaps, following the foundational principles of amorphous cell construction.[36] This chain length is at the onset of the entangled regime for PE ($M_e \approx 1000-1300$ g/mol[38]) and is consistent with prior MD studies of gas transport in PE.[12,18,19] The resulting simulation box contained 5000 united-atom sites, with a cubic cell edge of approximately 52 Å.
2 **High-Pressure Compaction:** The system was heated to 500 K and compressed to 1000 atm. As demonstrated in recent benchmarks,[12] this high-pressure state forces the collapse of initial voids and accelerates chain relaxation dynamics beyond what is achievable at ambient pressure.
3 **Isobaric Cooling:** While maintaining high pressure (1000 atm), the system was cooled slowly to 298 K. This "quenching under pressure" technique ensures high packing efficiency and prevents the reformation of large free-volume cavities during solidification.[39]
4 **Relaxation:** Finally, the pressure was released to 1 atm, and the system was equilibrated for 5 ns.

This protocol yielded pure-polymer amorphous matrices with an average density of $\rho_{pure} = 0.814 \pm 0.001$ g cm^{-3} at 298 K and 1 atm (averaged over the three independent structural realizations, Seeds A, B and C, before gas insertion; the per-seed values 0.8128, 0.8146, and 0.8154 g cm^{-3} are reported in Section 3). This value is slightly lower than the experimental density of high-molecular-weight amorphous PE (~0.85 g cm^{-3}), a well-known consequence of the disparate cooling rates between MD simulations (~10^{11} K/min) and experimental processing. It nevertheless represents a noticeable improvement over standard equilibration protocols, which report lower densities of ~0.795 g cm^{-3}[12] or ~0.805 g cm^{-3}.[19]

2.4. Gas Insertion and System Composition

Following equilibration, gas molecules were inserted into the relaxed polymer matrix using a random insertion algorithm with overlap rejection (minimum squared distance of 4.0 Å^2 for H_2 and 9.0 Å^2 for CH_4 from any existing atom). Two system types were prepared for each seed:

- **Mixed system (Mix):** 20 hydrogen molecules (H_2, 40 H atoms) and 20 methane molecules (CH_4) were inserted simultaneously, yielding 5060 total atoms. This configuration allows direct assessment of the relative transport of both species within the same polymer matrix under identical thermodynamic conditions.
- **Hydrogen-only system (H_2-only):** 20 hydrogen molecules were inserted without methane, for comparison with the mixed case.

The resulting gas concentrations correspond to approximately 0.058 wt % H_2 and 0.64 wt % CH_4 in the mixed system. For context, experimental Henry's law solubilities at 298 K and 1 atm in amorphous PE are approximately 0.01−0.05 wt % for H_2 and 0.2−0.5 wt % for CH_4.[9,11] Our loadings are thus within the same order of magnitude as equilibrium solubility under near-ambient conditions, confirming that the concentrations are physically reasonable. At these dilute loadings, direct gas−gas interactions are negligible, and the transport of each species is primarily governed by gas-polymer interactions. The number of molecules was chosen to provide sufficient statistical sampling of hopping events while maintaining the dilute limit, following the approach of Divine-Ayela et al.[18] A representative cross section of one of the equilibrated mixed simulation cells is shown in Figure 1, with H_2 and CH_4 molecules occupying distinct free-volume cavities within the dense polyethylene matrix. Upon gas insertion and subsequent NPT re-equilibration at 298 K and 1 atm, the matrix density of the mixed system reaches $\rho_{Mix,NPT} = 0.803 \pm 0.001$ g/cm^3, a ~1.4% reduction relative to the pure-polymer reference value of 0.814 ± 0.001 g/cm^3 (Section 3). This modest swelling confirms that the dilute mixed loading does not significantly perturb the matrix structure. We note that a rigorous determination of equilibrium solubility at specified thermodynamic conditions would require Grand Canonical Monte Carlo (GCMC) or Widom test-particle insertion methods, which are beyond the scope of the present diffusivity-focused study.

2.5. Transport Properties Analysis

Diffusion coefficients (D) for hydrogen and methane were extracted from the mean squared displacement (MSD) of the penetrants using the Einstein relation.[27] The self-diffusion coefficient is defined as

$$D = \lim_{t\to\infty} \frac{1}{6t}\langle|\mathbf{r}_i(t) - \mathbf{r}_i(0)|^2\rangle \quad (3)$$

https://doi.org/10.1021/acsapm.6c00287
ACS Appl. Polym. Mater. 2026, 8, 8017−8031

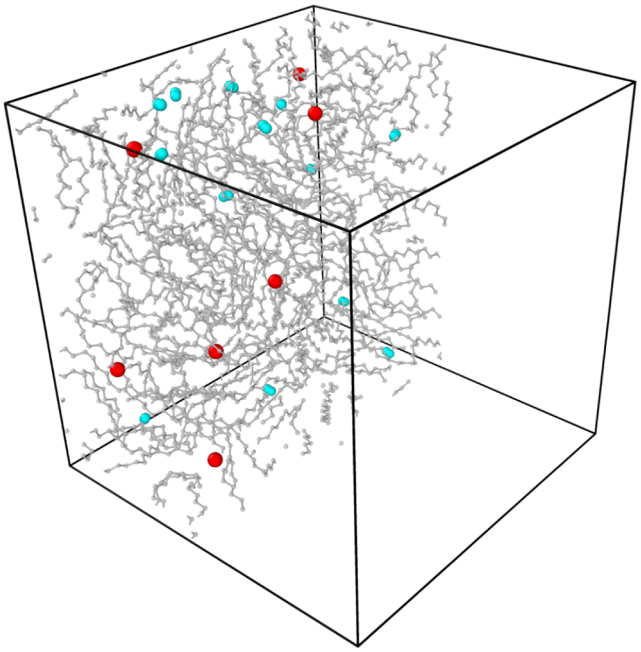

Figure 1. Cross-sectional view of the equilibrated simulation domain under standard conditions (NPT, 298 K). The slicing plane reveals the internal distribution of penetrant molecules within the dense amorphous polyethylene matrix (gray chains). Methane molecules (CH_4) are highlighted in red, and hydrogen (H_2) in cyan, occupying distinct free-volume cavities. The black bounding box represents the periodic boundary conditions.

where $\mathbf{r}_i(t)$ represents the unwrapped position vector of the center of mass of molecule i at time t. The value of D is determined from the slope (α) of the MSD linear regression in the diffusive regime ($D = \alpha/6$).

To rigorously identify the diffusive regime, we monitored the local slope of the MSD in a log−log plot (see Figure 7). Normal Fickian diffusion corresponds to a slope of $n \approx 1$, indicating that gas molecules are successfully hopping between adjacent pores.[12] In contrast, regimes with $n < 1$ (anomalous diffusion) reflect cage-rattling dynamics, while $n > 1$ corresponds to short-time ballistic motion. Following best practices for computing transport properties,[40] linear fitting was restricted to time intervals where $n \approx 1$ (typically $t > 1$ ns).

All NPT production simulations were performed at a target pressure of $P = 1$ atm (0.101325 MPa), controlled via the Nosé−Hoover barostat. This pressure represents ambient conditions and serves as a baseline for understanding intrinsic diffusive behavior. We note that operational pressures in gas distribution networks range from 4 to 80 bar, and hydrogen transmission pipelines may operate at even higher pressures. At elevated pressures, enhanced gas solubility and pressure-induced densification of the polymer matrix would alter transport dynamics; the present 1 atm simulations therefore characterize diffusive behavior decoupled from pressure-enhanced solubility effects.

To ensure sufficient sampling, data were collected from 48 independent production runs (3 structural realizations × 2 systems × 2 ensembles × 4 temperatures). The final diffusion coefficients are reported as the average over the 3 independent seeds, with error bars representing the standard deviation.

Potential finite-size effects were assessed using the Yeh−Hummer correction:[41] $D_{corr} = D_{PBC} + k_B T\xi/(6\pi\eta L)$, where $\xi = 2.837$, $L \approx 52$ Å is the box edge length, and η is the polymer matrix viscosity. For a dense polymer melt with $\eta \sim 1-10$ Pa·s, the correction term is of order 10^{-8} to 10^{-7} cm^2/s, which is less than 1% of the computed diffusivities and well within the statistical uncertainty. Therefore, finite-size corrections were not applied.

The membrane separation literature defines the ideal permselectivity as the ratio of permeabilities:

$$\alpha_P = \frac{P_{H_2}}{P_{CH_4}} = \frac{D_{H_2}}{D_{CH_4}} \times \frac{S_{H_2}}{S_{CH_4}} = \alpha_D \times \alpha_S \quad (4)$$

where α_D is the diffusivity selectivity and α_S is the solubility selectivity. Since the present equilibrium MD simulations do not include a direct calculation of solubility (which would require GCMC or Widom insertion methods), we report only the diffusivity selectivity α_D:

$$\alpha_D = \frac{D_{H_2}}{D_{CH_4}} \quad (5)$$

This quantity isolates the kinetic sieving contribution to separation performance. For H_2/CH_4 in polyethylene, $S_{CH_4} > S_{H_2}$ (methane is more condensable and thus more soluble due to stronger van der Waals interactions with the polymer matrix), meaning that $\alpha_S < 1$. Consequently, the permeability selectivity α_P is expected to be lower than the diffusivity selectivity α_D reported here.[11] Error bars on α_D were computed via standard error propagation: $\delta\alpha_D/\alpha_D = \sqrt{(\delta D_{H_2}/D_{H_2})^2 + (\delta D_{CH_4}/D_{CH_4})^2}$.

3. RESULTS AND DISCUSSION

3.1. Structural Characterization and Validation of the Amorphous Matrix

Prior to analyzing gas transport properties, it is imperative to verify that the generated polyethylene matrices represent a realistic equilibrated amorphous state, devoid of crystalline artifacts or residual voids associated with insufficient relaxation.

Figure 2 presents the Carbon−Carbon Radial Distribution Function, $g_{C-C}(r)$, averaged over the final equilibration trajectories at 298 K. The profile exhibits a sharp primary peak at 1.54 Å, corresponding to the covalent bond length constrained by the harmonic potential. This is followed by secondary peaks characteristic of local angular and torsional ordering.

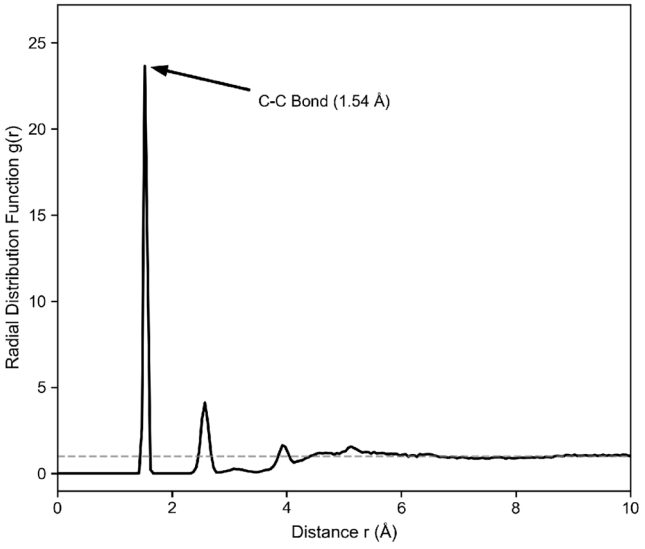

Figure 2. Carbon−carbon Radial Distribution Function, $g_{C-C}(r)$, for the equilibrated polyethylene matrix at 298 K. The rapid convergence to unity ($g(r) \approx 1$ for $r > 10$ Å) confirms the absence of periodic lattice correlations characteristic of crystalline structures, validating the amorphous nature of the sample.

Crucially, for distances $r > 6$ Å, the function decays rapidly to unity ($g(r) \rightarrow 1$). In crystalline solids, the lattice periodicity causes peaks to persist over long distances. In contrast, the

https://doi.org/10.1021/acsapm.6c00287
ACS Appl. Polym. Mater. 2026, 8, 8017−8031

Table 2. Free-Volume Metrics of the Equilibrated Polyethylene Matrix from Random-Probe Insertion (4×10^5 Probes per Snapshot, 10 Frames per Trajectory, 3 Independent Seeds)[a]

Ensemble	T (K)	ρ (g/cm^3)	FV_0 (%)	FV_{H_2}(%)	FV_{CH_4}(%)	FV_{H_2}/FV_{CH_4}	LCD (Å)	PLD (Å)
NPT	298	0.803	39.4	0.48 ± 0.02	0.06 ± 0.01	8.2	5.24	1.35
NPT	323	0.783	41.1	0.69 ± 0.06	0.10 ± 0.02	7.1	5.50	1.53
NPT	348	0.764	42.4	0.97 ± 0.06	0.16 ± 0.02	6.0	5.76	1.67
NPT	373	0.745	43.9	1.34 ± 0.06	0.27 ± 0.02	5.0	6.44	1.74
NVT	298	0.819	38.3	0.36 ± 0.02	0.03 ± 0.01	10.2	5.00	1.29
NVT	323	0.819	38.4	0.35 ± 0.02	0.03 ± 0.00	10.4	5.01	1.32
NVT	348	0.819	38.4	0.35 ± 0.01	0.03 ± 0.00	10.7	4.93	1.32
NVT	373	0.819	38.4	0.35 ± 0.01	0.03 ± 0.00	10.6	5.01	1.32

[a]FV_0 is the matrix void fraction (probe radius 0); FV_{H_2} and FV_{CH_4} are the fractions accessible to probes of radius 1.45 and 1.90 Å, respectively. LCD and PLD are the largest cavity diameter and pore limiting diameter (see text). Density is the production-run average of the mix system.

convergence to unity observed here indicates that the local density at long-range becomes uniform and indistinguishable from the bulk average, signifying a complete loss of positional correlation. This structural feature confirms that the multistage high-pressure annealing protocol successfully generated an isotropic and fully disordered amorphous morphology.

The calculated density of the equilibrated pure polymer matrices at 298 K and 1 atm was $\rho_{pure} = 0.814 \pm 0.001$ g cm^{-3} (averaged over Seeds A, B and C, before gas insertion). The corresponding Mix systems were prepared by inserting 20 H_2 and 20 CH_4 molecules into the same equilibrated boxes; this brings two distinct effects depending on the production ensemble:

- In *NPT*, the Parrinello−Rahman barostat is free to relax the box volume after the insertion, and the matrix expands slightly to accommodate the dilute gas loading. The production-run density therefore drops to $\rho_{Mix,NPT} = 0.803 \pm 0.001$ g cm^{-3}, a ∼1.4% swelling relative to the pure-polymer baseline.
- In *NVT*, the box volume is held fixed at the equilibrated pure-polymer reference value by construction, while the system mass increases by the mass of the inserted H_2 and CH_4 molecules ($M_{H_2} + M_{CH_4}$ in total). The density is therefore mechanically forced to rise to $\rho_{Mix,NVT} = 0.819 \pm 0.003$ g cm^{-3}, ∼0.6% above the pure-polymer reference. This is the value reported as the NVT line in Figure 10, and the offset between $\rho_{pure} = 0.814$ and $\rho_{Mix,NVT} = 0.819$ is fully accounted for by the added gas mass at constant volume.

The two ensembles thus probe two different but well-defined points along the same matrix's $\rho-T$ plane, with the NPT branch tracking thermal expansion and the NVT branch fixed at the high-density extreme; this is exactly the contrast that drives the ensemble-dependent selectivity discussed in Sections 3.7 and 3.8.

While these simulated densities are lower than the experimental value for high-molecular-weight amorphous PE ($\rho_{exp} \approx 0.85$ g cm^{-3}), the discrepancy is a well-known consequence of the disparity between MD cooling rates (∼10^{11} K/min) and experimental processing rates: even the most carefully equilibrated MD models of PE typically settle within the 0.78−0.84 g cm^{-3} window. Among recent UA studies, Zheng et al.[12] reported ∼0.795 g cm^{-3} and Dutta and Bhatia[19] ∼0.805 g cm^{-3}; densities closer to experiment have been obtained with longer chain lengths and slower cooling protocols, e.g. Sun et al.[42] (∼0.84 g cm^{-3}) and Hussain et al.[43] for HDPE-like models of semicrystalline PE. Atiq et al.[44] reported similarly close-to-experiment values for explicitly semicrystalline PE built from ordered tie-chain regions. We acknowledge that this 4−5% density gap is the principal source of the systematic 1−2 order-of-magnitude overprediction of the absolute diffusivities discussed in Section 3.6; importantly, however, the *ensemble-dependent selectivity trade-off* that is the central result of this work depends on the *derivative* response of the matrix to thermal expansion versus volumetric confinement, which is captured correctly by the force field even when the absolute baseline density is shifted.

3.2. Free Volume Characterization: Pore Size Distribution, PLD, and LCD

To resolve the microstructural basis of the ensemble-dependent selectivity, we performed a free-volume analysis using the random-probe insertion method that has become standard for amorphous polymer membranes.[45,46] For each polymer configuration we placed 4×10^5 random test points inside the simulation cell and, applying the minimum-image convention, computed the *insertion radius* at every point as

$$r_{ins}(\mathbf{x}) = \min_{i \in poly} \left[|\mathbf{x} - \mathbf{x}_i| - \frac{\sigma_i}{2} \right] \quad (6)$$

where σ_i is the Lennard-Jones diameter of polymer atom i ($\sigma_{CH_3} = 3.75$ Å, $\sigma_{CH_2} = 3.95$ Å). $r_{ins}(\mathbf{x})$ is the radius of the largest hard sphere that can be centered at $\mathbf{x}$ without overlapping the van der Waals surface of any polymer site. Probe points falling *inside* a polymer atom give $r_{ins} < 0$ and are unphysical: they correspond to the occupied volume of the matrix and are excluded from the pore size distribution (PSD). With this convention, a probe of radius zero is accepted everywhere outside the solid, the cumulative distribution at $r_{ins} = 0^+$ equals unity over the void space, and the analysis is consistent with the implementations used by Heuchel et al.[46] and the geometry-based pore analysis tools of Willems et al.[47] Statistics were accumulated over 10 evenly spaced frames extracted from the second half of each production trajectory and averaged over the three independent seeds, giving an effective sample size of 1.2×10^7 probe points per thermodynamic state.

In addition to the standard accessible free-volume fraction $FV(r_{probe}) = Pr[r_{ins} \geq r_{probe}]$, we report the two geometry-based metrics commonly used in the porous-materials literature:[47]

- the **Largest Cavity Diameter** (LCD) $= 2\max_{\mathbf{x}} r_{ins}(\mathbf{x})$, the diameter of the largest spherical pocket present in the matrix, and
- the **Pore Limiting Diameter** (PLD), the largest probe diameter for which the set $\{\mathbf{x}: r_{ins}(\mathbf{x}) \geq r_{probe}\}$ still

https://doi.org/10.1021/acsapm.6c00287
ACS Appl. Polym. Mater. 2026, 8, 8017−8031

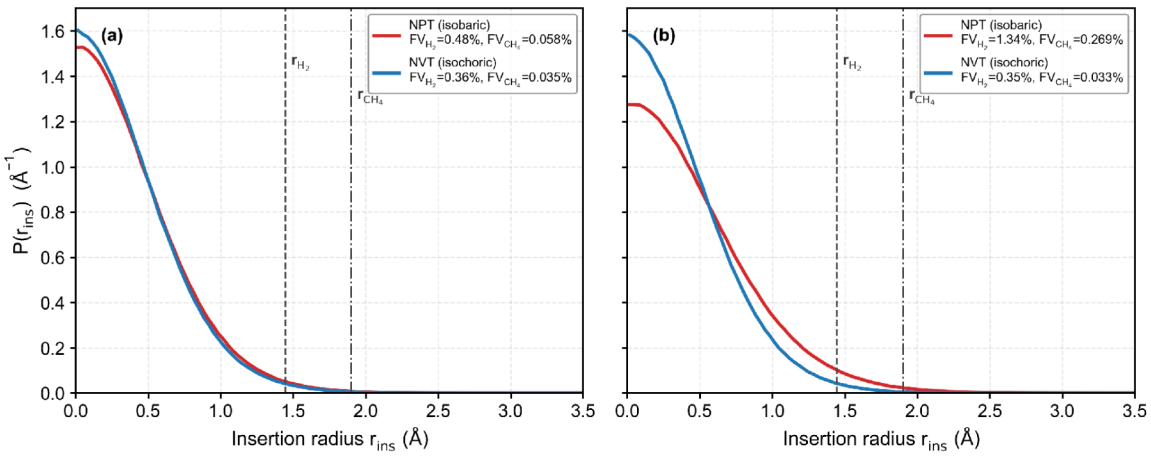

Figure 3. Pore size distribution $P(r_{ins})$ of the amorphous polyethylene matrix at (a) 298 K and (b) 373 K, comparing NPT (red) and NVT (blue) ensembles. Probe points lying inside the van der Waals surface of any polymer atom ($r_{ins} < 0$) are excluded; the histograms are normalized over the void space so that a probe of radius zero is accepted everywhere outside the solid. Vertical dashed and dot−dashed lines mark the effective H_2 and CH_4 probe radii (1.45 and 1.90 Å). At 298 K both ensembles share the equilibrium density and produce nearly identical distributions; at 373 K the NPT distribution develops a distinct heavy tail, while the NVT distribution is essentially unchanged.

percolates across the periodic cell. The PLD was obtained by evaluating r_{ins} on a regular 1 Å grid and identifying the largest probe radius for which a connected-component cluster touched opposite faces of the cubic box.[47]

The four free-volume quantities (FV_0, FV_{H_2}, FV_{CH_4}, LCD and PLD) are gathered in Table 2, and the corresponding pore size distributions at 298 and 373 K are shown in Figure 3. At 298 K, the NPT and NVT distributions are essentially indistinguishable: both ensembles share the equilibrium ∼0.81 g cm^{-3} density and an overall void fraction $FV_0 \approx 38-39\%$. At 373 K a clear divergence appears: thermal expansion under NPT lowers the matrix density to 0.745 g cm^{-3}, FV_0 rises to 43.9%, the PSD develops a distinct heavy tail, and the LCD grows from 5.24 to 6.44 Å. Under volumetric confinement (NVT) the same temperature change leaves ρ, FV_0, the PSD, the LCD (∼5 Å) and the PLD (∼1.3 Å) statistically unchanged within seed-to-seed scatter. The vertical markers in Figure 3 indicate the effective probe radii for H_2 (r = 1.45 Å, kinetic diameter 2.89 Å) and CH_4 (r = 1.90 Å, kinetic diameter 3.80 Å); the heavy-tail growth at 373 K NPT explicitly raises both gas-accessible fractions and constitutes the structural fingerprint of the ensemble-dependent selectivity discussed in Section 3.7.

It is worth emphasizing that the static-snapshot PLD (∼1.3−1.7 Å) is consistently smaller than the kinetic diameter of either gas (2.89 Å for H_2, 3.80 Å for CH_4). This is the geometric counterpart of the activated-hopping picture: at any given instant, the static free-volume network is not directly percolating for either penetrant, and gas transport is enabled by transient bottleneck openings driven by thermal motion of the polymer chains.[17,18,22] The fact that the LCD (∼5 Å NVT, up to 6.4 Å NPT) substantially exceeds both kinetic diameters indicates that, although individual cavities can comfortably host either molecule, hopping between cavities is the rate-limiting elementary step of diffusion.

The temperature dependence of the gas-accessible free volume is shown in Figure 4. Under NPT, FV_{H_2} grows by a factor of ∼2.8 (0.48% → 1.34%) and FV_{CH_4} by a factor of ∼4.5 (0.06% → 0.27%); the disproportionate growth of the methane-accessible fraction is the structural origin of the loss of size-sieving with temperature. Under NVT both fractions are flat

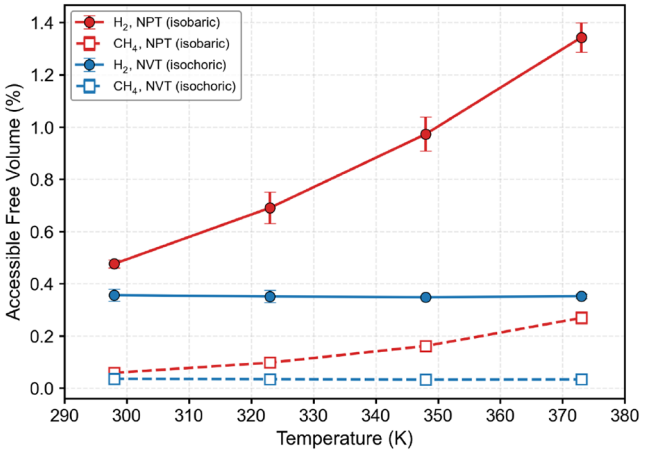

Figure 4. Temperature dependence of the accessible free volume for H_2 (filled markers, solid lines) and CH_4 (open markers, dashed lines) probes under NPT (red) and NVT (blue) ensembles. Error bars are the standard deviation over the three independent seeds. Under NPT both fractions grow with temperature, with the CH_4-accessible fraction growing relatively faster; under NVT both fractions are statistically constant.

within the seed-to-seed uncertainty, confirming that volumetric confinement preserves the size-sieving character of the free-volume network across the full temperature range. The temperature dependence of the LCD and PLD (Figure 5) reinforces the same picture: in NPT the LCD grows from 5.2 to 6.4 Å and the PLD from 1.35 to 1.74 Å, while in NVT both are flat at ∼5.0 and ∼1.31 Å, respectively.

3.3. Microscopic Basis of Selectivity: Steric Exclusion and Free Volume Theory

The disparate transport behaviors of hydrogen and methane originate primarily from their molecular size difference. According to the free volume theory proposed by Cohen and Turnbull,[48] molecular transport in amorphous media occurs via the statistical redistribution of free volume (V_f). Diffusion is only possible if a local void exceeds a critical volume (v^*) sufficient to accommodate the penetrant. Since v^* is intrinsically governed by the molecular size of the solute, the probability of finding a

https://doi.org/10.1021/acsapm.6c00287
ACS Appl. Polym. Mater. 2026, 8, 8017−8031

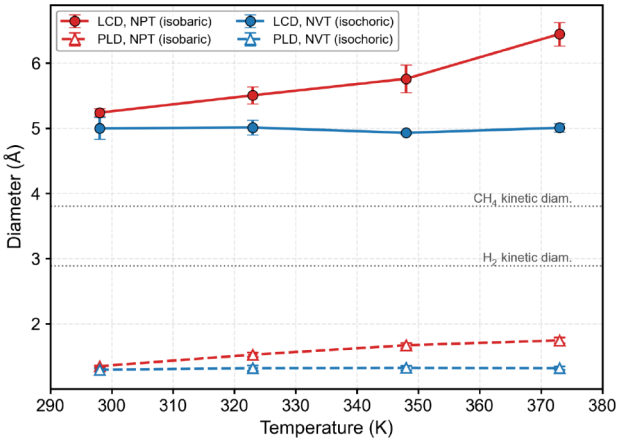

Figure 5. Largest Cavity Diameter (LCD, filled circles) and Pore Limiting Diameter (PLD, open triangles) of the amorphous polyethylene matrix as a function of temperature, computed from the random-probe and grid percolation analyses (see text). Horizontal dotted lines mark the kinetic diameters of H_2 and CH_4. The static PLD lies well below either kinetic diameter, consistent with thermally activated hopping as the elementary transport mechanism.

hole large enough for CH_4 is exponentially lower than for H_2, as quantified in Table 2.

To quantify this steric exclusion, we analyzed the local environment of the penetrants. Figure 6 displays the probability distribution of the minimum distance between the center of mass of a gas molecule and the nearest polymer atom. A clear separation is observed: the distribution for hydrogen peaks at ≈3.35 Å, whereas methane peaks at ≈3.75 Å. This shift reflects the smaller van der Waals radius of hydrogen, allowing it to access interstitial sites and narrow channels that are sterically forbidden to methane.[12]

This differential accessibility dictates the dynamic mechanism. Hydrogen, being less restricted by the polymer boundaries, follows an ″activated hopping″ mechanism.[18] It spends short residence times in local voids before executing rapid jumps to adjacent cavities, consistent with the free-volume formulations for diffusion in polymers described by Fujita.[49] In favorable configurations involving aligned polymer chains, H_2 may even undergo ″skipping″ motions—long, uninterrupted displacements akin to diffusion in a tunnel—facilitated by its minute cross-section.[18]

In contrast, the larger methane molecule is strongly confined by the surrounding polymer structure. Its dynamics are characterized by prolonged ″rattling″ within singular low-density cages.[18] Unlike hydrogen, which percolates through the existing static free volume, methane diffusion is heavily dependent on the cooperative motion of the polymer chains to open transient bottlenecks.[37] This explains the higher activation energy observed for methane and why its transport is so sensitive to the density reduction (swelling) under NPT conditions.

3.4. Transport Mechanism: Activated Hopping and Cage Dynamics

The dynamic behavior of the penetrants is characterized by the Mean Squared Displacement (MSD), as shown in Figure 7. Both species undergo Fickian diffusion at long time scales, but their microscopic transport mechanisms differ fundamentally. Three characteristic dynamic regimes are observed: a short ballistic regime at $t < 1$ ps, a transitionary "caging" regime where particles rattle within free-volume pockets, and a final diffusive regime for $t > 100$ ps.

The long-time slope for both H_2 and CH_4 converges to unity ($n \approx 1$ in the log−log plot), confirming normal Fickian diffusion.[12] This validates the extraction of diffusion coefficients using the Einstein relation. The clear separation between the MSD curves reflects the differential kinetic accessibility of the polymer free-volume network: hydrogen, with its smaller kinetic diameter (~2.89 Å),[50] navigates the polymer matrix via rapid jumps between adjacent cavities (activated hopping), whereas methane (~3.8 Å) is predominantly confined to cage-rattling dynamics within individual cavities, requiring cooperative

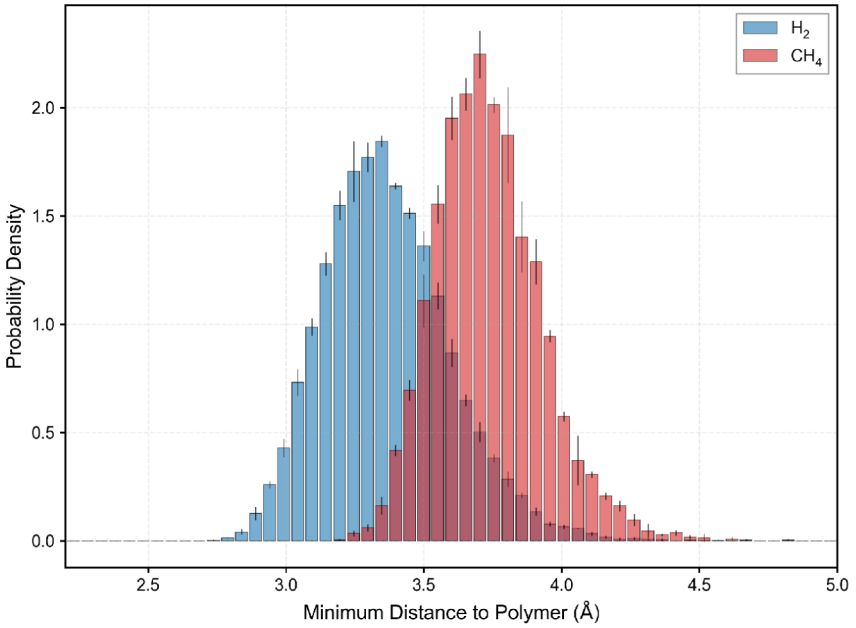

Figure 6. Distribution of minimum distances between gas molecules and the polymer backbone. The shift of ~0.4 Å between H_2 and CH_4 quantifies the steric exclusion effect: H_2 can access smaller interstitial sites (v^*) that are inaccessible to CH_4.

https://doi.org/10.1021/acsapm.6c00287
ACS Appl. Polym. Mater. 2026, 8, 8017−8031

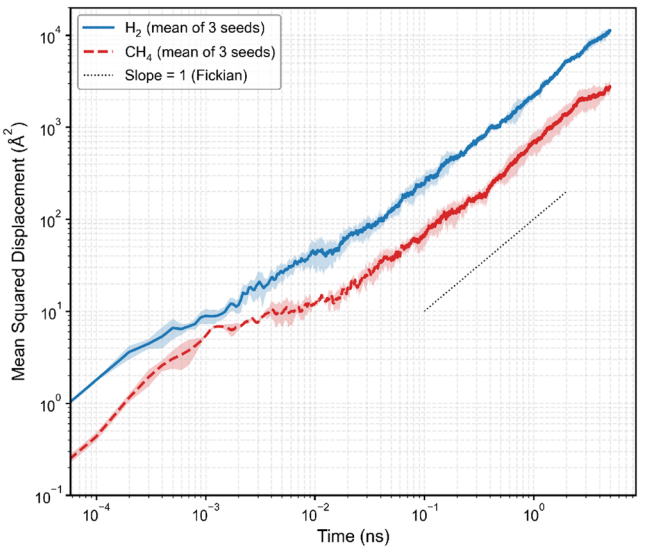

Figure 7. Log−log plot of the Mean Squared Displacement (MSD) for H_2 and CH_4 at 298 K. The transition to the Fickian diffusive regime (slope ≈ 1) is observed after approximately 0.1 ns.

polymer chain motion to transition between sites.[18] Both mechanisms constitute forms of diffusion; the distinction lies in the frequency and length scale of the elementary transport events.

To examine the microscopic mechanism, Figure 8 analyzes the frame-to-frame displacement distribution. Methane dynamics are dominated by a narrow peak at small displacements (<3 Å), indicating that CH_4 molecules spend most of the time trapped in local cages ("rattling"). In contrast, hydrogen exhibits a "heavy tail" extending beyond 10 Å. This confirms that transport proceeds via an *activated hopping* mechanism,[12,17,22] where small H_2 molecules vibrate within a pore for an extended period before executing rare, rapid jumps to adjacent cavities. These jumps are facilitated by transient channels opened by the thermal motion of the polymer chains,[18] a pathway that remains sterically forbidden for the larger methane molecules on these time scales.

3.5. Thermal Swelling and Activation Energy

The temperature dependence of diffusivity was analyzed under both isobaric (NPT) and isochoric (NVT) ensembles. As shown in Figure 9, the diffusion coefficients follow Arrhenius behavior

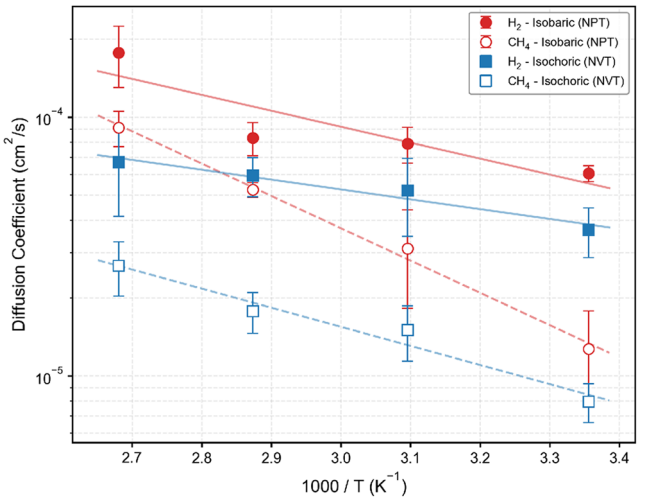

Figure 9. Arrhenius plot of diffusion coefficients for H_2 and CH_4 in the mixed system under NPT (red) and NVT (blue) ensembles. Solid lines: H_2; dashed lines: CH_4. Thin lines represent linear regression fits from which activation energies were extracted. Error bars represent the standard deviation over 3 independent seeds.

($D = D_0\, e^{-E_a/RT}$) across the studied range (298 K−373 K), with linear regression fits on the semilogarithmic plot yielding $R^2 > 0.95$ for CH_4 and for H_2 under NVT conditions. The lower $R^2 = 0.80$ obtained for H_2 under NPT reflects the weaker temperature dependence of hydrogen diffusivity in the thermally expanded matrix: because H_2 is small enough to percolate through the existing free-volume network, the additional free volume created by thermal expansion provides only a modest incremental benefit, resulting in a flatter Arrhenius slope that is more sensitive to statistical scatter over the four temperature points. Methane exhibits a steeper slope than hydrogen, indicating a higher activation energy (E_a), consistent with the experimental

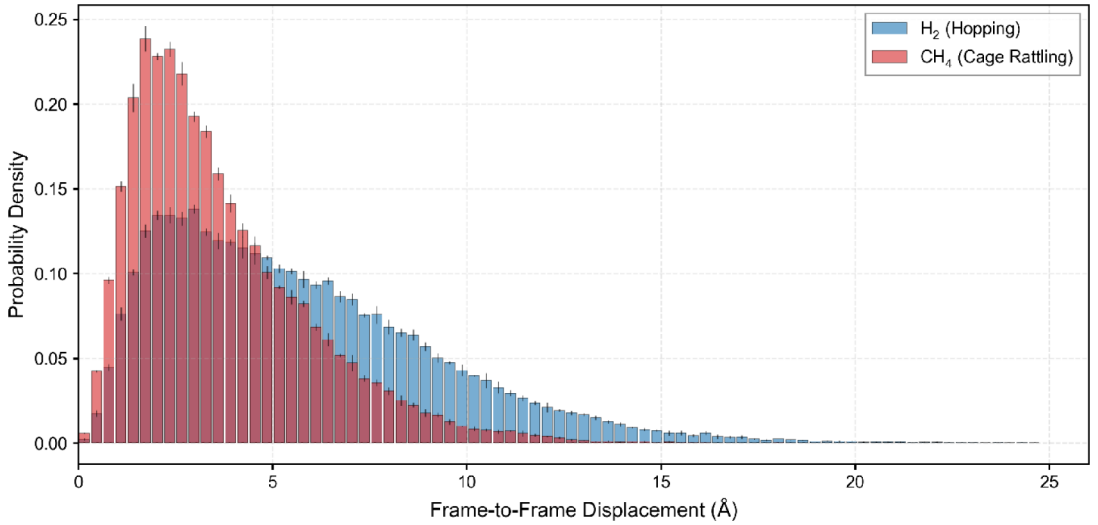

Figure 8. Distribution of frame-to-frame displacements. The "heavy tail" for H_2 (blue) confirms a hopping mechanism, whereas CH_4 (orange) remains kinetically trapped in local cages.

https://doi.org/10.1021/acsapm.6c00287
ACS Appl. Polym. Mater. 2026, 8, 8017−8031

measurements of Barrer for polyolefins.[51,52] The energy barrier is linked to the energy required to create a hole of sufficient size in the matrix.[12]

A fundamental divergence is observed between ensembles. NPT simulations consistently yield higher diffusivities than NVT simulations at temperatures above 298 K. This is explained by the thermal expansion of the matrix, as quantified in Figure 10. Under NPT conditions, density decreases linearly with

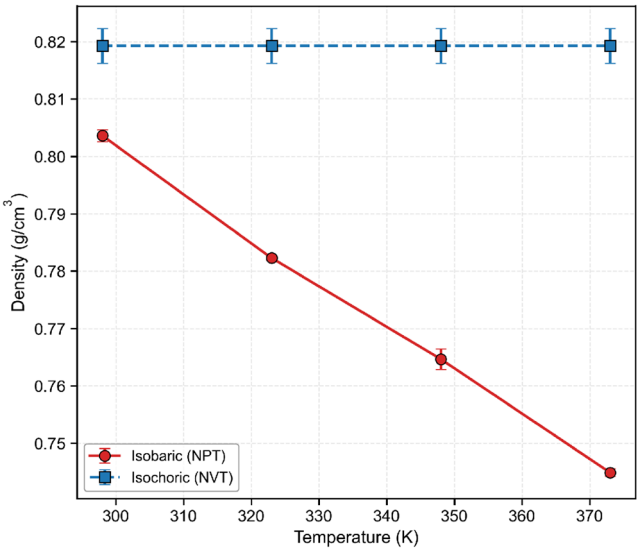

Figure 10. Temperature dependence of the polymer matrix density under NPT (red) and NVT (blue) ensembles. The linear decrease under NPT reflects thermal expansion, while NVT maintains the 298 K density by construction.

temperature ($R^2 > 0.999$), generating additional free volume that facilitates transport.[17] From the linear fit of the NPT density data for the mixed system, the volumetric thermal expansion coefficient is $\alpha_V = -(1/\rho)(d\rho/dT) \approx 9.5 \times 10^{-4}$ K^{-1}. This value is approximately 30% higher than the experimental value for fully amorphous PE ($\alpha_V \approx 7.2 \times 10^{-4}$ K^{-1}),[53] consistent with the lower simulated density providing a larger free-volume fraction and thus greater thermal expansivity. The apparent activation energy under constant pressure therefore includes a contribution from the thermally driven expansion of the free-volume network, whereas under constant volume, it reflects only the intrinsic energetic barrier for hopping.

The extracted activation energies are presented in Table 3. Under NVT conditions, $E_a(CH_4) > E_a(H_2)$, consistent with the larger critical hole volume required for methane transport. The

Table 3. Activation Energies (E_a) Extracted from Arrhenius Fits of the Diffusion Coefficient Data ($D = D_0\, e^{-E_a/RT}$) for H_2 and CH_4 in the Mixed System under NPT and NVT Ensembles, Compared with Experimental Ranges Reported for Semicrystalline Polyethylene

Gas	Ensemble/Source	E_a (kJ/mol)	R^2/Notes
H_2	NPT (this work)	11.8	0.80
H_2	NVT (this work)	7.3	0.95
H_2	Experimental (lit.)[9,11]	25−40	LDPE−HDPE
CH_4	NPT (this work)	23.9	0.99
CH_4	NVT (this work)	14.1	0.96
CH_4	Experimental (lit.)[9,11]	35−55	LDPE−HDPE

NPT activation energies are higher than their NVT counterparts for both gases, reflecting the additional free-volume expansion contribution. These values can be compared with the experimental activation energies compiled by Michaels and Bixler[11] and reviewed by Klopffer and Flaconnèche[9] for semicrystalline polyethylene, which span the ranges $E_a(H_2) \approx$ 25−40 kJ/mol and $E_a(CH_4) \approx$ 35−55 kJ/mol going from low-density to high-density PE. Our computed values are systematically lower than these experimental ranges. This underestimation is attributed to three factors: (i) the lower simulated density ($\rho \approx 0.80$ g/cm^3 vs experimental ~0.85 g/cm^3) provides a larger free-volume fraction and thus a smaller energetic penalty for cavity formation; (ii) the united-atom representation produces a smoother effective potential energy surface, reducing intramolecular friction that would slow penetrant jumps in all-atom or experimental systems; and (iii) the experimental values correspond to semicrystalline PE, in which the crystalline phase introduces additional transport barriers absent in the fully amorphous model. Importantly, the relative ordering $E_a(CH_4) > E_a(H_2)$ and the trend $E_a(NPT) > E_a(NVT)$ are both physically consistent, confirming that the model correctly captures the underlying transport physics.

3.6. Comparison with Experimental and Computational Benchmarks

To validate the simulation framework, Table 4 compares the computed diffusion coefficients and diffusivity selectivities with both computational and experimental literature values. We emphasize from the outset that for H_2/CH_4 separation in polyethylene the diffusivity selectivity $\alpha_D = D_{H_2}/D_{CH_4}$ and the experimental permeability selectivity $\alpha_P = \alpha_D \times \alpha_S$ obey the relation $\alpha_P < \alpha_D$, because methane is the more soluble (more condensable) component and consequently $\alpha_S = S_{H_2}/S_{CH_4} < 1$.[9,11,54] The diffusivity values discussed below were originally reported by Michaels and Bixler in their companion "Flow of gases through polyethylene" paper,[54] and the corresponding solubility data in their "Solubility of gases in polyethylene" paper;[11] we cite both throughout. The relevant comparison for our diffusivity-only data is against experimental *diffusivity* selectivities (rather than permeability selectivities), since we do not compute solubilities.

The computed self-diffusion coefficients are 1−2 orders of magnitude larger than the experimental values for semicrystalline PE. This systematic overprediction is the combined consequence of three well-understood effects: (a) the simulated density (0.80−0.82 g cm^{-3}) is lower than experimental amorphous PE (~0.85 g cm^{-3}) because of the disparity between MD and experimental cooling rates, leaving the matrix with more free volume than the real polymer; (b) the fully amorphous model deliberately omits the crystalline lamellae that introduce a tortuosity factor τ^2 in semicrystalline PE, so the experimental D_{eff} in HDPE is geometrically reduced by 1−2 orders of magnitude relative to the amorphous baseline;[11,25] (c) the united-atom representation produces a smoother effective potential energy surface than all-atom force fields, slightly reducing intramolecular friction. Recent MD studies that target denser matrices, with longer chains and slower cooling protocols (Sun et al.[42]), or that explicitly construct semicrystalline morphologies and tie-chain regions (Atiq et al.;[44] Hussain et al.[43]), routinely achieve ρ_{sim} values in the 0.84−0.96 g cm^{-3} range and the corresponding H_2 diffusivities are systematically lower and closer to experiment, confirming that closing the density gap is the single most effective route toward realistic

https://doi.org/10.1021/acsapm.6c00287
ACS Appl. Polym. Mater. 2026, 8, 8017−8031

Table 4. Diffusion Coefficients and Diffusivity Selectivities ($\alpha_D = D_{H_2}/D_{CH_4}$) of H_2 and CH_4 in Polyethylene at ~298−303 K[a]

Source	Material	$D(H_2)$ (cm^2/s)	$D(CH_4)$ (cm^2/s)	α_D	Method
This work (NPT)	Amorphous PE	6.1×10^{-5}	1.3×10^{-5}	4.8	MD, TraPPE-UA
This work (NVT)	Amorphous PE	3.7×10^{-5}	7.9×10^{-6}	4.6	MD, TraPPE-UA
Divine-Ayela (2023)[18]	Amorph. PE	$\sim 5 \times 10^{-5}$	–	–	MD (AA)
Dutta & Bhatia (2017)[19]	Amorph. PE	$\sim 1 \times 10^{-5}$	$\sim 1 \times 10^{-6}$	~10	MD (AA)
Zheng et al. (2022)[12]	Amorph. PE	$\sim 3 \times 10^{-5}$	–	–	MD (TraPPE)
Michaels & Bixler (1961)[54]	LDPE	$\sim 6 \times 10^{-7}$	$\sim 1 \times 10^{-7}$	~5−7	Experimental
Klopffer (2001)[9]	HDPE	$\sim 4 \times 10^{-8}$	$\sim 5 \times 10^{-9}$	~8−10	Experimental

[a]Experimental sources report permeability selectivities α_P; the corresponding α_D values, where available, are listed separately. Notethat for H_2/CH_4 in PE $\alpha_S < 1$ and consequently $\alpha_P < \alpha_D$.

absolute diffusivities. This is an important caveat for the absolute values reported here, and it directly motivates our framing of the present work as a study of the *differential* response of a single, well-equilibrated amorphous matrix to the NPT vs NVT thermomechanical boundary conditions, rather than as a benchmark of absolute permeability.

A second observation, which concerns the diffusivity selectivity rather than the absolute values, is encouraging. The experimental diffusivity selectivity for H_2/CH_4 in polyethylene compiled across a range of grades and primary sources[9,54] typically lies in the band $\alpha_D^{exp} \approx 5 - 12$, going from amorphous-rich LDPE to highly crystalline HDPE. Our simulated $\alpha_D \approx 4.6-4.8$ at 298 K therefore sits at the *low end* of the experimental range and is consistent in magnitude with experimental amorphous-rich PE measurements, even though the absolute D values are systematically overpredicted by 1−2 orders of magnitude because of the low simulated density. This is an important sanity check on the force field: the matrix is too loose to reproduce experimental *absolute* mobilities but it is dense enough to reproduce the experimental *ratio* of mobilities to within a factor of order unity.

For completeness, the Michaels and Bixler solubility paper[11] reports $S_{H_2}/S_{CH_4} \approx 0.1 - 0.2$ (methane is the more condensable component, dissolving 5−10× more than hydrogen at 25 °C), and Klopffer's review[9] reports experimental permeability selectivities in the range $\alpha_P^{exp} \approx 1 - 3$ for LDPE and $\alpha_P^{exp} \approx 5 - 10$ for highly crystalline HDPE. The relation $\alpha_P = \alpha_D \times \alpha_S$ is thus only approximate when one combines values from different primary sources and PE grades, but the qualitative ordering $\alpha_P < \alpha_D$ holds robustly for this gas pair: our $\alpha_D \approx 5$ combined with $\alpha_S \approx 0.1-0.2$ predicts $\alpha_P \approx 0.5-1$, which is about a factor of 2−4 below the experimental amorphous-PE permeability selectivity $\alpha_P^{exp} \approx 1 - 3$. The remaining factor-of-2−4 gap is again traceable to the lower simulated density: a denser matrix would shift both gases along the same Cohen−Turnbull master curve (Section 3.8), reducing both absolute diffusivities and amplifying the size-sieving advantage of H_2, which would simultaneously raise α_D and α_P toward the experimental ranges.

3.7. Ensemble-Dependent Diffusivity Selectivity

The interplay between thermal activation and free volume leads to one of the central findings of this work, presented in Figure 12a. Under NPT conditions, the H_2/CH_4 diffusivity selectivity decreases from $\alpha_D \approx 4.8$ at 298 K to $\alpha_D \approx 1.9$ at 373 K; the trajectory is nonmonotonic, reaching a minimum of ~1.6 at 348 K before recovering slightly at 373 K. The nonmonotonic behavior lies within the statistical uncertainty (error bars overlap at the two highest temperatures) and likely reflects the limited

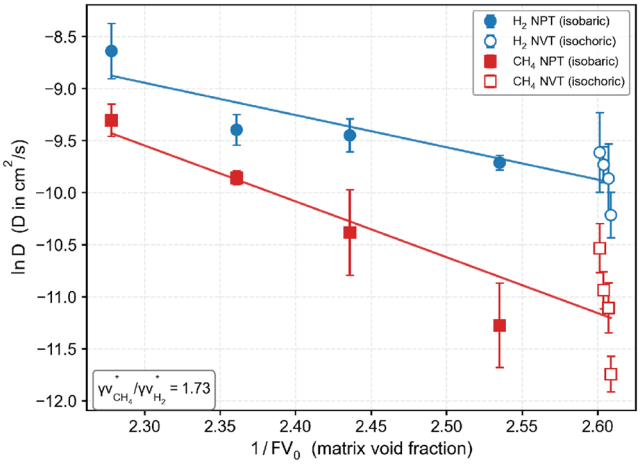

Figure 11. Cohen−Turnbull plot of ln D versus $1/FV_0$ (matrix void fraction) for H_2 (blue circles) and CH_4 (red squares). Filled markers: NPT; open markers: NVT. Each gas obeys a single Cohen−Turnbull line that pools both ensembles, with $R^2 \approx 0.78$. The slope ratio $\gamma v^*_{CH_4}/\gamma v^*_{H_2} \approx 1.73 \approx (\sigma_{CH_4}/\sigma_{H_2})^2$ is consistent with the size-of-bottleneck rather than the volume-of-cavity scaling of the activation parameter.

sampling of rare hopping events for CH_4 at elevated temperatures. The overall trend indicates that thermal expansion disproportionately enhances the diffusivity of the larger penetrant, eroding the kinetic sieving ability of the polymer matrix. This is the molecular-level counterpart of the well-known trade-off between permeability and selectivity in polymer membranes.[55,56]

Under volumetrically confined NVT conditions, the diffusivity selectivity decreases much more gradually, from $\alpha_D \approx 4.6$ at 298 K to $\alpha_D \approx 2.5$ at 373 K. By suppressing the expansion of the free-volume network—as quantified directly in Table 2 and Figures 4 and 5—the confined matrix maintains a substantially larger steric exclusion against methane across the entire temperature range.

We stress that the values 2−5 quoted here are *diffusivity* selectivities α_D and not permeability selectivities α_P. Experimental diffusivity selectivities for H_2/CH_4 in polyethylene typically lie in the band $\alpha_D^{exp} \approx 5 - 12$, going from amorphous-rich LDPE to highly crystalline HDPE, while the corresponding permeability selectivities lie in the band $\alpha_P^{exp} \approx 1 - 10$ over the same range.[9,11,54] The relation $\alpha_P = \alpha_D \times \alpha_S$ holds with $\alpha_S = S_{H_2}/S_{CH_4} \approx 0.1 - 0.5$ depending on grade, so $\alpha_P < \alpha_D$ for this gas pair; combining our $\alpha_D \approx 5$ with $\alpha_S \approx 0.1-0.2$ would give $\alpha_P \approx 0.5-1$, a factor of 2−4 below the experimental band. As discussed in Section 3.6, our simulated $\alpha_D \approx 5$ at 298 K

https://doi.org/10.1021/acsapm.6c00287
ACS Appl. Polym. Mater. 2026, 8, 8017−8031

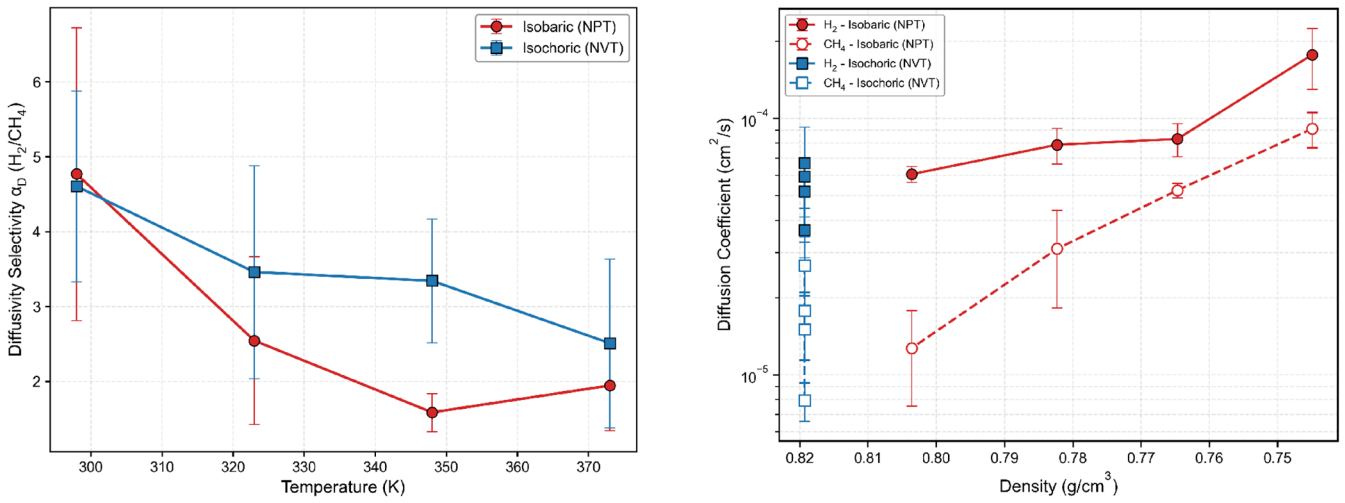

(a) Diffusivity selectivity (α_D) vs. temperature. (b) Diffusion coefficients vs. matrix density.

Figure 12. (a) Ensemble-dependent diffusivity selectivity: volumetric confinement (NVT, blue) retains higher selectivity relative to unconstrained expansion (NPT, red) across the temperature range, though both ensembles show a decrease with temperature. Error bars represent propagated uncertainty from the standard deviation of 3 independent seeds. (b) Diffusion coefficients plotted against polymer matrix density, illustrating the stronger sensitivity of CH_4 to free-volume changes compared to H_2.

already sits at the low end of the experimental band; the additional factor that would close the residual gap toward the higher experimental α_P is again the lower simulated density, which would reduce both absolute diffusivities and amplify the size-sieving advantage of H_2. The physically meaningful comparison in this work is therefore the *relative* response of α_D to the NPT vs NVT boundary conditions, which is robust against the absolute density baseline and which the Cohen–Turnbull master curve of Section 3.8 captures quantitatively.

Figure 12b unifies these observations by plotting diffusivity directly against density. Two distinct regimes emerge: under NVT conditions, density is fixed and diffusion is driven solely by thermal activation (kinetic energy), producing a "vertical" trajectory on the D-ρ plot. Under NPT conditions, diffusion is driven by the combined effects of thermal activation and free-volume expansion, yielding a "sloped" trajectory. The steeper slope observed for methane in the NPT regime confirms its stronger sensitivity to free-volume fluctuations,[17] providing the physical basis for the selectivity reduction in thermally expanded systems.

3.8. Quantitative Connection to Cohen–Turnbull Free-Volume Theory

The ensemble-dependent diffusivity selectivity can be rationalized quantitatively in the framework of Cohen–Turnbull free-volume theory.[48,49] In its standard form,

$$D = D_0 \exp\left(-\gamma \frac{v^*}{v_f}\right) \tag{7}$$

the diffusion coefficient depends exponentially on the ratio of the critical hole volume v^* required to accommodate the penetrant to the mean free volume per matrix segment v_f, with $\gamma \in [0.5, 1]$ an overlap factor and D_0 a pre-exponential factor related to the molecular velocity. Because v^* depends on the gas but v_f is a property of the polymer matrix, eq 7 predicts that, on a single matrix subjected to different thermomechanical conditions, ln D should fall on a straight line when plotted against $1/v_f$, with a gas-specific slope $-\gamma v^*$.

In the present work, the matrix free volume is directly observable: we identify v_f with the void fraction FV_0 measured in Section 3.2 (more precisely, with the polymer-segment-specific volume $V_{box}\,FV_0/N_{seg}$, but absorbing the constant prefactor into the slope). Figure 11 plots ln D versus $1/FV_0$ for the eight Mix simulations (four temperatures × two ensembles) for both H_2 and CH_4. Three observations stand out:

(1) For each gas, the NPT and NVT data points fall on the same Cohen–Turnbull line (filled and open markers in Figure 11). The two ensembles produce different absolute values of D at the same temperature precisely because they probe different points along a single underlying $D(FV_0)$ master curve (Figure 11). This is direct evidence that the apparent ensemble dependence of α_D is the consequence of free-volume modulation, not of two distinct microscopic mechanisms. We note that the four NVT data points cluster tightly around $1/FV_0 \approx 2.61$—as they must, since the NVT void fraction is fixed by construction at ∼38.4% and only varies with temperature through the residual chain dynamics; the NPT branch, in contrast, sweeps the range $1/FV_0 \approx 2.28$–2.54. The Cohen–Turnbull line is therefore effectively anchored by the four NPT points and corroborated by the (nearly degenerate) NVT cluster, rather than by eight independent positions along the abscissa. This is consistent with the physical interpretation: a single matrix property (FV_0) controls the diffusivity, and the role of the NVT cluster is to test whether the line extrapolates correctly to the high-density end of the matrix-density range.

(2) The slopes of the two fits, $-\gamma v^*$, are strongly gas-specific: −3.10 for H_2 and −5.36 for CH_4 (in units of inverse void fraction), with corresponding coefficients of determination $R^2 \approx 0.78$ for both gases. Given that each pooled fit contains only $n = 8$ points (4 NPT + 4 NVT) and that the rare-event hopping statistics of CH_4 have intrinsically larger relative uncertainties than those of H_2 (cf. Table 4 and the seed-resolved error bars on Figure 11), an R^2 of

https://doi.org/10.1021/acsapm.6c00287
ACS Appl. Polym. Mater. 2026, 8, 8017–8031

~0.78 is in fact a stringent rather than a mediocre fit: the residuals lie within the seed-to-seed standard deviation for every individual data point, and the Cohen−Turnbull description is statistically indistinguishable from a one-parameter Arrhenius fit on the same data.

(3) The slope ratio

$$\frac{(\gamma v^*)_{CH_4}}{(\gamma v^*)_{H_2}} \approx \frac{5.36}{3.10} \approx 1.73 \quad (8)$$

matches almost exactly the squared kinetic-diameter ratio $(\sigma_{CH_4}/\sigma_{H_2})^2 = (3.80/2.89)^2 \approx 1.73$, but is significantly smaller than the cubed ratio $(\sigma_{CH_4}/\sigma_{H_2})^3 \approx 2.27$ that would be expected if v^* scaled with the molecular volume. The empirical d^2 scaling of γv^* is consistent with the picture that the activation barrier for hopping is set by the cross-sectional area of the bottleneck the penetrant must traverse, rather than by the cavity volume needed to host it—in agreement with the surface-of-cavity activation model proposed by Freeman[56] for the permeability-selectivity trade-off in glassy polymers.

The activation energies extracted from the Arrhenius fits (Table 3) carry the same physical content from a different angle. The higher E_a for CH_4 relative to H_2 in both ensembles reflects the larger energetic barrier associated with finding (or thermally creating) a cavity sufficient to accommodate methane. The difference between NPT and NVT activation energies is particularly pronounced for CH_4 ($E_a^{NPT}/E_a^{NVT} \approx 1.7$), confirming that a significant fraction of the apparent NPT activation energy is the heat of expansion of the free-volume network rather than an intrinsic barrier-crossing energy. The fact that the same activation-energy ordering and ratio are recovered from two complementary analyses—the Arrhenius fits in Table 3 and the Cohen−Turnbull line in Figure 11—provides an internal consistency check on the free-volume interpretation of the ensemble-dependent selectivity.

3.9. Boundary Condition Implications

The NPT and NVT ensembles represent two limiting thermomechanical boundary conditions that a polymer may experience. The NPT ensemble corresponds to unconstrained expansion, as would occur in a polymer liner free to swell. The NVT ensemble represents the limit of perfect volumetric confinement, which may arise in any scenario where the polymer matrix is mechanically restrained-for example, by crystalline lamellae in semicrystalline PE, by rigid housings in compressed joints, or by reinforcing fillers.[23]

It is important to emphasize that the NVT results presented here do not directly model specific elastomeric seals, which possess distinct chemistry (e.g., cross-linked EPDM, NBR, or FKM rubbers), cross-link networks, and filler distributions that fundamentally alter their free-volume structure and transport properties. The NVT ensemble is employed here strictly as a thermodynamic limiting case of perfect volumetric confinement for amorphous polyethylene, not as a quantitative model for any specific seal material. Within this scope, the results demonstrate the general physical principle that volumetric confinement mitigates the loss of diffusivity selectivity by suppressing the free-volume dilation that disproportionately enhances methane transport. This finding is qualitatively consistent with the observed durability of high-pressure seals in experimental studies where volumetric expansion is restricted.[13,57] The behavior of real semicrystalline PE components likely lies between the NPT and NVT limits, with crystalline constraints partially restricting the expansion of the amorphous phase. Quantitative predictions for specific seal materials would require dedicated simulations with material-specific force fields and cross-linked network models.

4. LIMITATIONS AND OUTLOOK

While the presented framework provides statistically grounded insights into gas diffusion mechanisms, several limitations of the model should be noted.

First, this study focuses exclusively on diffusivity and does not compute solubility coefficients. A complete assessment of permeability ($P = S \times D$) would require Grand Canonical Monte Carlo (GCMC) simulations or Widom test-particle insertion to determine Henry's law constants. Consequently, the diffusivity selectivity values reported here ($\alpha_D \approx 2-5$) should be interpreted in light of the relation $\alpha_P = \alpha_D \times \alpha_S$, with $\alpha_S \approx 0.1-0.5$ for H_2/CH_4 in PE so that $\alpha_P < \alpha_D$ for this gas pair, and not directly compared against experimental permeability selectivities ($\alpha_P^{exp} \approx 1-10$, going from LDPE to HDPE) without accounting for α_S. Computing solubility coefficients and the full permeability selectivity is an important direction for future work.

Second, the use of a United-Atom (UA) force field, while computationally efficient for extensive sampling, treats hydrogen atoms along the polymer backbone as implicit. This results in a smoother effective potential surface compared to All-Atom (AA) models. Although TraPPE-UA accurately reproduces liquid densities and phase equilibria, the reduced intramolecular friction could lead to slightly faster dynamics for very small penetrants like H_2. However, comparative studies suggest that relative trends in selectivity and density dependence remain consistent between UA and AA representations.[20]

Third, the simulated density of the Mix systems ($\rho_{Mix,NPT} \approx 0.803$, $\rho_{Mix,NVT} \approx 0.819$ g cm^{-3}, both 4−5% below the ~0.85 g cm^{-3} experimental value for fully amorphous PE) is the dominant origin of the systematic 1−2 order-of-magnitude overprediction of the absolute diffusion coefficients reported in Table 4. This density gap is the well-documented consequence of the disparity between MD cooling rates (~10^{11} K/min) and experimental processing rates, and recent literature shows it can be reduced by combining longer chains, slower cooling and different force fields,[42−44] although typically at the cost of substantially more compute. Hierarchical equilibration strategies employing coarse-grained models followed by reverse-mapping to united-atom resolution[20] are an additional promising route. Crucially, the ensemble-dependent selectivity trade-off that we report arises from the *derivative* response of the matrix (thermal expansion vs volumetric confinement), and the Cohen−Turnbull collapse of Figure 11 shows that the same master curve $D(FV_0)$ controls both ensembles. The specific values of α_D would shift along this master curve in a denser matrix, but the qualitative ensemble dependence—and the squared-kinetic-diameter slope ratio—are robust against the absolute density baseline.

Fourth, the present study employs chains of 100 carbon atoms (C_{100}), corresponding to a molecular weight of approximately $M_w \approx 1400$ g/mol. This chain length is at the onset of the entangled regime for polyethylene ($M_e \approx 1000-1300$ g/mol[38]). Longer chains would increase the entanglement density, potentially reducing chain mobility and free-volume fluctuations, which could decrease gas diffusivity. However, the choice

https://doi.org/10.1021/acsapm.6c00287
ACS Appl. Polym. Mater. 2026, 8, 8017−8031

of C_{100} is consistent with prior MD studies of gas transport in PE,[12,18,19] where chains of similar length were shown to yield converged density and transport properties. A systematic study of chain-length dependence on H_2/CH_4 selectivity remains an important direction for future work.

Fifth, real pipeline materials are semicrystalline. In semicrystalline PE, the crystalline lamellae are essentially impermeable to light gases and act as physical barriers that increase the effective diffusion path length by a tortuosity factor τ. The effective diffusivity is then $D_{eff} = D_{amorphous}/\tau^2$, where τ depends on the crystalline volume fraction and lamellar morphology. For typical HDPE ($\phi_c \sim 0.6-0.7$), this yields D_{eff} values 1−2 orders of magnitude lower than $D_{amorphous}$, which is consistent with the difference between our computed values and experimental diffusivities reported in Table 4. The crystalline lamellae also act as physical cross-links that partially restrict the swelling of the amorphous phase even under isobaric conditions. Therefore, our NPT results represent a limiting case of unrestricted expansion, while the NVT results represent perfect confinement. The behavior of real semicrystalline PE components likely lies between these two limits. Future work incorporating semicrystalline morphologies is required to quantify the role of crystalline constraints in bridging these regimes.

Finally, diffusion coefficients in MD simulations with periodic boundary conditions are subject to finite-size effects.[41] As discussed in Section 2, the Yeh−Hummer correction for our system is less than 1% of the computed diffusivities. A full convergence study with different box sizes was not performed but is not expected to alter the conclusions, given the magnitude of the correction relative to the statistical uncertainty.

5. CONCLUSIONS

In this work we have developed and validated a fully open-source Molecular Dynamics framework to quantify the *diffusive* transport of hydrogen and methane in amorphous polyethylene. Combining a multistage high-pressure annealing protocol with extensive statistical sampling (48 production runs across 3 seeds, 4 temperatures and 2 thermodynamic ensembles), we have produced well-equilibrated amorphous matrices ($\rho_{pure} = 0.814 \pm 0.001$ g cm^{-3}, $\rho_{Mix,NPT} = 0.803$, $\rho_{Mix,NVT} = 0.819$ g cm^{-3}) and statistically converged diffusion coefficients with seed-resolved error bars, and characterized the underlying free-volume network with the standard porous-materials descriptors LCD and PLD.

Trajectory analysis revealed fundamentally different microscopic transport mechanisms for the two penetrants. Hydrogen navigates the polymer free-volume network via activated hopping—rapid jumps between adjacent cavities characterized by a broad ("heavy-tailed") displacement distribution. Methane dynamics are dominated by prolonged cage-rattling within individual cavities, requiring cooperative polymer chain motion to transition between sites. Both mechanisms constitute Fickian diffusion at long time scales, and the differential accessibility of the free-volume network gives a diffusivity selectivity $\alpha_D \approx 4.6-4.8$ at 298 K. Importantly, the static-snapshot Pore Limiting Diameter (∼1.3−1.7 Å) lies well below the kinetic diameter of either gas, providing a direct geometric corroboration of the activated-hopping picture: the static free-volume network is not directly percolating, and transport relies on transient bottleneck openings.

The central, novel finding of this work is the existence of an *ensemble-dependent diffusivity-selectivity trade-off* for H_2/CH_4 in amorphous PE, a phenomenon that prior computational studies—almost all of them performed exclusively in NPT and on a single gas at a time—could not have detected. Under isobaric (NPT) conditions, thermal expansion lowers the matrix density from 0.803 to 0.745 g cm^{-3}, raises the void fraction from 39.4 to 43.9% and the LCD from 5.24 to 6.44 Å, and reduces α_D from ∼4.8 to ∼1.9 between 298 and 373 K. Under volumetrically confined (NVT) conditions, the matrix density is held fixed, the LCD and PLD are temperature-independent within seed-to-seed scatter, and α_D decreases far more slowly, from ∼4.6 to ∼2.5 over the same range. This is the molecular-level expression of the well-known permeability−selectivity trade-off,[55,56] isolated for the first time in a controlled MD comparison on the same polymer matrix.

A second, equally important contribution is that the entire NPT/NVT data set collapses onto a single Cohen−Turnbull master curve per gas when ln D is plotted against $1/FV_0$ (Figure 11). The slopes of the two master lines, $\gamma v^*_{H_2}$ and $\gamma v^*_{CH_4}$, satisfy a ratio of 1.73, which agrees almost exactly with $(\sigma_{CH_4}/\sigma_{H_2})^2 = 1.73$ but not with $(\sigma_{CH_4}/\sigma_{H_2})^3 = 2.27$. This empirical d^2 scaling of the Cohen−Turnbull activation parameter—which to our knowledge has not been reported before for H_2/CH_4 in PE—directly supports the size-of-bottleneck picture of activated diffusion proposed by Freeman,[56] in which the activation barrier scales with the cross-sectional area of the channel the penetrant must traverse rather than with the volume of the cavity that hosts it. Beyond its mechanistic interest, the collapse establishes that the apparent ensemble dependence of α_D is wholly governed by free-volume modulation: a quantitative bridge between the macroscopic NPT/NVT boundary condition, the directly measurable matrix free volume, and the microscopic Cohen−Turnbull activation parameter.

We are explicit about the limitations that frame these contributions. The simulated densities are 4−5% lower than experiment, and consequently the absolute D values are systematically overpredicted by 1−2 orders of magnitude relative to experimental semicrystalline PE (Section 3.6). The values reported here should therefore not be used as benchmarks of absolute permeability; the relevant claims are the *differential* response of α_D to NPT vs NVT, the Cohen−Turnbull master curve and its slope ratio, and the geometric LCD/PLD analysis of the free-volume network. We further distinguish carefully between the diffusivity selectivity α_D and the experimental permeability selectivity $\alpha_P = \alpha_D \times \alpha_S$: for H_2/CH_4 in PE methane is the more soluble component, $\alpha_S < 1$, and consequently $\alpha_P < \alpha_D$. Our simulated $\alpha_D \approx 5$ at 298 K already lies at the low end of the experimental band $\alpha_D^{exp} \approx 5 - 12$ for polyethylene,[9,54] so the simulation is in fact in approximate agreement with experiment for the diffusivity *ratio*; the residual factor-of-2−4 gap toward the higher experimental α_P values is again traceable to the lower simulated density, which would slide both gases along the same Cohen−Turnbull master line.

From a practical perspective, these results demonstrate that the thermomechanical boundary conditions experienced by a polymer component—whether it is free to swell or volumetrically confined by crystalline lamellae, rigid housings or reinforcing fillers—have a quantifiable, monotonic and Cohen−Turnbull-predictable effect on its kinetic sieving behavior. Coupling this NPT/NVT framework to GCMC solubility calculations, semicrystalline morphologies, and validation against permeability measurements at elevated

https://doi.org/10.1021/acsapm.6c00287
ACS Appl. Polym. Mater. 2026, 8, 8017−8031

H_2NG operating pressures are the natural next steps toward engineering-grade simulation predictions.

■ ASSOCIATED CONTENT

Data Availability Statement

All simulation input files (LAMMPS scripts for polymer generation, high-pressure annealing, gas insertion, and production runs), analysis scripts (MSD computation, diffusion coefficient extraction, pore size distribution, and figure generation), and representative output data are freely available in the associated GitHub repository (https://github.com/danieldelgadouriarte/pe-h2-ch4-md). The complete simulation workflow is documented to enable full reproducibility, in accordance with FAIR data management principles.

Supporting Information

The Supporting Information is available free of charge at https://pubs.acs.org/doi/10.1021/acsapm.6c00287.

Animations of H_2 molecular trajectories within the amorphous PE matrix under NPT and NVT conditions at selected temperatures (MP4)

Animations of CH_4 molecular trajectories within the amorphous PE matrix under NPT and NVT conditions at selected temperatures; these animations illustrate the activated hopping mechanism of H_2 and the cage-rattling dynamics of CH_4 discussed in Section 3 (MP4)

■ AUTHOR INFORMATION

Corresponding Authors

Daniel Delgado-Uriarte − *Facultad de Ingenieria, Universidad de Deusto, Bilbao, Bizkaia 48007, Spain;* orcid.org/0009-0006-0536-5158; Email: danieldelgadouriarte@gmail.com

Alejandro Lopez − *Facultad de Ingenieria, Universidad de Deusto, Bilbao, Bizkaia 48007, Spain;* orcid.org/0000-0001-5498-1746; Email: alejandro.lopez@deusto.es

Complete contact information is available at: https://pubs.acs.org/10.1021/acsapm.6c00287

Author Contributions

D.D.-U.: Conceptualization, methodology, software, formal analysis, writing—original draft, visualization. A.L.: Supervision, writing—review & editing.

Notes

The authors declare no competing financial interest.

■ ACKNOWLEDGMENTS

The authors acknowledge Universidad de Deusto, Facultad de Ingenieria, for providing computational resources. This research did not receive any specific grant from funding agencies in the public, commercial, or not-for-profit sectors.

■ REFERENCES

(1) Melaina, M. W.; Antonia, O.; Penev, M.. *Blending Hydrogen into Natural Gas Pipeline Networks: A Review of Key Issues*; National Renewable Energy Laboratory, 2013.

(2) European Commission. *A Hydrogen Strategy for a Climate-Neutral Europe*; European Commission, 2020.

(3) Hydrogen Council. *Path to Hydrogen Competitiveness: A Cost Perspective*; Hydrogen Council, 2020.

(4) International Energy Agency. *Global Hydrogen Review 2023*; IEA, https://www.iea.org/reports/global-hydrogen-review-2023, 2023; Accessed 13 April 2026.

(5) Mahajan, D.; Tan, K.; Venkatesh, T.; Kileti, P.; Clayton, C. R. Hydrogen Blending in Gas Pipeline Networks-A Review. *Energies* **2022**, *15*, 3582.

(6) San Marchi, C.; Somerday, B. P.. *Technical Reference for Hydrogen Compatibility of Materials. Nonmetals: Polymers (Code 8100)*; Sandia National Laboratories, 2012;.

(7) Campari, A.; Ustolin, F.; Alvaro, A.; Paltrinieri, N. A review on hydrogen embrittlement and risk-based inspection of hydrogen technologies. *Int. J. Hydrogen Energy* **2023**, *48*, 35316−35346.

(8) Raj, A.; Larsson, I. A. S.; Ljung, A.-L.; Forslund, T.; Andersson, R.; Sundström, J.; Lundström, T. S. Evaluating hydrogen gas transport in pipelines: Current state of numerical and experimental methodologies. *Int. J. Hydrogen Energy* **2024**, *67*, 136−149.

(9) Klopffer, M. H.; Flaconnèche, B. Transport Properties of Gases in Polymers: Bibliographic Review. *Oil Gas Sci. Technol.* **2001**, *56*, 223−244.

(10) Hmaimid, Z.; Thoppurathu Varghese, R.; Finger, D. C.; Gudlaugsson, B.; Costa, D. A.; Ahmed, T.; Arackal Narayanan, J. A Comprehensive Review on the Compatibility of Polymeric Materials for Hydrogen Transportation and Storage. *Int. J. Hydrogen Energy* **2025**, *192*, 152366.

(11) Michaels, A. S.; Bixler, H. J. Solubility of Gases in Polyethylene. *J. Polym. Sci.* **1961**, *50*, 393−412.

(12) Zheng, D.; Li, J.; Liu, B.; Yu, B.; Yang, Y.; Han, D.; Li, J.; Huang, Z. Molecular dynamics investigations into the hydrogen permeation mechanism of polyethylene pipeline material. *J. Mol. Liq.* **2022**, *368*, 120773.

(13) Fujiwara, H.; Ono, H.; Ohyama, K.; Kasai, M.; Kaneko, F.; Nishimura, S. Hydrogen permeation under high pressure conditions and the destruction of exposed polyethylene-property of polymeric materials for high-pressure hydrogen devices (2). *Int. J. Hydrogen Energy* **2021**, *46*, 11832−11848.

(14) Yamabe, J.; Nishimura, S. Influence of fillers on hydrogen penetration properties and blister fracture of rubber composites for O-ring exposed to high-pressure hydrogen gas. *Int. J. Hydrogen Energy* **2009**, *34*, 1977−1989.

(15) Wijmans, J. G.; Baker, R. W. The solution-diffusion model: a review. *J. Membr. Sci.* **1995**, *107*, 1−21.

(16) Müller-Plathe, F. Molecular Dynamics Simulation of Gas Transport in Amorphous Polypropylene. *J. Chem. Phys.* **1992**, *96*, 3200−3205.

(17) Takeuchi, H.; Okazaki, K. Molecular dynamics simulation of diffusion of simple gas molecules in a short chain polymer. *J. Chem. Phys.* **1990**, *92*, 5643−5652.

(18) Divine-Ayela, C.; Perez, F.; Striolo, A. Hop, Skip, and Jump: Hydrogen Molecular Transport through Amorphous Polyethylene Matrices Studied via Molecular Dynamics Simulations. *Ind. Eng. Chem. Res.* **2023**, *62*, 19893−19906.

(19) Dutta, R. C.; Bhatia, S. K. Transport diffusion of light gases in polyethylene using atomistic simulations. *Langmuir* **2017**, *33*, 936−946.

(20) Spyriouni, T.; Tzoumanekas, C.; Theodorou, D.; Müller-Plathe, F.; Milano, G. Coarse-Grained and Reverse-Mapped United-Atom Simulations of Long-Chain Atactic Polystyrene Melts: Structure, Thermodynamic Properties, Chain Conformation, and Entanglements. *Macromolecules* **2007**, *40*, 3876−3885.

(21) Vrentas, J. S.; Duda, J. L. Diffusion in polymer-solvent systems. I. Reexamination of the free-volume theory. *J. Polym. Sci. Polym. Phys. Ed.* **1977**, *15*, 403−416.

(22) Gusev, A. A.; Müller-Plathe, F.; van Gunsteren, W. F.; Suter, U. W. *Advances in Polymer Science*; Springer: Berlin, Heidelberg, 1994 Vol. *116*, pp 207−247.

(23) Minelli, M.; Sarti, G. C. Elementary prediction of gas permeability in glassy polymers. *J. Membr. Sci.* **2017**, *521*, 73−83.

(24) Martin, M. G.; Siepmann, J. I. Transferable potentials for phase equilibria. 1. United-atom description of n-alkanes. *J. Phys. Chem. B* **1998**, *102*, 2569−2577.

(25) Nielsen, L. E. Models for the Permeability of Filled Polymer Systems. *J. Macromol. Sci., Part A: Chem.* **1967**, *1*, 929−942.

(26) Plimpton, S. Fast parallel algorithms for short-range molecular dynamics. *J. Comput. Phys.* **1995**, *117*, 1−19.
(27) Allen, M. P.; Tildesley, D. J. *Computer Simulation of Liquids*; Oxford University Press, 2017.
(28) Tamai, Y.; Tanaka, H.; Nakanishi, K. Molecular simulation of permeation of small penetrants through membranes. 1. Diffusion coefficients. *Macromolecules* **1994**, *27*, 4498−4508.
(29) Frenkel, D.; Smit, B. *Understanding Molecular Simulation: from Algorithms to Applications*; Academic Press, 2002.
(30) Nosé, S. A unified formulation of the constant temperature molecular dynamics methods. *J. Chem. Phys.* **1984**, *81*, 511−519.
(31) Hoover, W. G. Canonical dynamics: Equilibrium phase-space distributions. *Phys. Rev. A* **1985**, *31*, 1695−1697.
(32) Parrinello, M.; Rahman, A. Polymorphic transitions in single crystals: A new molecular dynamics method. *J. Appl. Phys.* **1981**, *52*, 7182−7190.
(33) Delhommelle, J.; Millié, P. Inadequacy of the Lorentz-Berthelot combining rules for accurate predictions of equilibrium properties by molecular simulation. *Mol. Phys.* **2001**, *99*, 619−625.
(34) Jorgensen, W. L.; Maxwell, D. S.; Tirado-Rives, J. Development and Testing of the OPLS All-Atom Force Field on Conformational Energetics and Properties of Organic Liquids. *J. Am. Chem. Soc.* **1996**, *118*, 11225−11236.
(35) Tuckerman, M.; Berne, B. J.; Martyna, G. J. Reversible multiple time scale molecular dynamics. *J. Chem. Phys.* **1992**, *97*, 1990−2001.
(36) Theodorou, D. N.; Suter, U. W. Detailed molecular structure of a vinyl polymer glass. *Macromolecules* **1985**, *18*, 1467−1478.
(37) Kremer, K.; Grest, G. S. Dynamics of entangled linear polymer melts. *J. Chem. Phys.* **1990**, *92*, 5057−5086.
(38) Fetters, L. J.; Lohse, D. J.; Richter, D.; Witten, T. A.; Zirkel, A. Connection between polymer molecular weight, density, chain dimensions, and melt viscoelastic properties. *Macromolecules* **1994**, *27*, 4639−4647.
(39) Moyassari, A.; Mostafavi, H.; Gkourmpis, T.; Hedenqvist, M. S.; Gedde, U. W.; Nilsson, F. Simulation of semi-crystalline polyethylene: Effect of short-chain branching on tie chains and trapped entanglements. *Polymer* **2015**, *72*, 177−184.
(40) Maginn, E. J.; Messerly, R. A.; Carlson, D. J.; Roe, D. R.; Elliott, J. R. Best Practices for Computing Transport Properties 1. Self-Diffusivity and Viscosity from Equilibrium Molecular Dynamics [Article v1.0]. *Living J. Comp. Mol. Sci.* **2018**, *1*, 6324.
(41) Yeh, I.-C.; Hummer, G. System-size dependence of diffusion coefficients and viscosities from molecular dynamics simulations with periodic boundary conditions. *J. Phys. Chem. B* **2004**, *108*, 15873−15879.
(42) Sun, C.; Hou, C.; Zhang, Y. Molecular dynamic simulation of polyethylene chain at different temperatures and pressures. *Sustainable Energy Technol. Assess* **2022**, *52*, 102096.
(43) Hussain, M.; Yamamoto, T.; Adil, S.; Yao, S. Preparation and Characterization of High-Density Polyethylene with Alternating Lamellar Stems Using Molecular Dynamics Simulations. *Polymers* **2024**, *16*, 304.
(44) Atiq, O.; Ricci, E.; Baschetti, M. G.; De Angelis, M. G. Molecular Simulations of Hydrogen Sorption in Semicrystalline High-Density Polyethylene: The Impact of the Surface Fraction of Tie-Chains. *J. Phys. Chem. B* **2024**, *128*, 2799−2810.
(45) Hofmann, D.; Fritz, L.; Ulbrich, J.; Schepers, C.; Böhning, M. Detailed-atomistic molecular modeling of small molecule diffusion and solution processes in polymeric membrane materials. *Macromol. Theory Simul.* **2000**, *9*, 293−327.
(46) Heuchel, M.; Hofmann, D.; Pullumbi, P. Molecular Modeling of Small-Molecule Permeation in Polyimides and Its Correlation to Free-Volume Distributions. *Macromolecules* **2004**, *37*, 201−214.
(47) Willems, T. F.; Rycroft, C. H.; Kazi, M.; Meza, J. C.; Haranczyk, M. Algorithms and Tools for High-Throughput Geometry-Based Analysis of Crystalline Porous Materials. *Microporous Mesoporous Mater.* **2012**, *149*, 134−141.
(48) Cohen, M. H.; Turnbull, D. Molecular transport in liquids and glasses. *J. Chem. Phys.* **1959**, *31*, 1164−1169.
(49) Fujita, H. *Advances in Polymer Science*; Springer: Berlin, Heidelberg, 1961, Vol. *3*, pp 1−47.
(50) Breck, D. W.. *Zeolite Molecular Sieves*; John Wiley & Sons, 1974.
(51) Barrer, R. M.; Rideal, E. K. Permeation, Diffusion and Solution of Gases in Organic Polymers. *Trans. Faraday Soc.* **1939**, *35*, 628−643.
(52) Barrer, R. M. *Diffusion in and Through Solids*; Cambridge University Press: Cambridge, 1951.
(53) Van Krevelen, D. W.; Te Nijenhuis, K. *Properties of Polymers: Their Correlation with Chemical Structure*; Their Numerical Estimation and Prediction from Additive Group Contributions; Elsevier, 2009.
(54) Michaels, A. S.; Bixler, H. J. Flow of Gases through Polyethylene. *J. Polym. Sci.* **1961**, *50*, 413−439.
(55) Robeson, L. M. Correlation of Separation Factor versus Permeability for Polymeric Membranes. *J. Membr. Sci.* **1991**, *62*, 165−185.
(56) Freeman, B. D. Basis of permeability/selectivity tradeoff relations in polymeric gas separation membranes. *Macromolecules* **1999**, *32*, 375−380.
(57) Yamabe, J.; Koga, A.; Nishimura, S. Failure behavior of rubber O-ring under cyclic exposure to high-pressure hydrogen gas. *Eng. Fail. Anal.* **2013**, *35*, 193−205.

https://doi.org/10.1021/acsapm.6c00287
ACS Appl. Polym. Mater. 2026, 8, 8017−8031